JACS
JOURNAL OF THE AMERICAN CHEMICAL SOCIETY
pubs.acs.org/JACS
Article

Driving Barocaloric Effects in a Molecular Spin-Crossover Complex at Low Pressures

Jinyoung Seo,[†] Jason D. Braun,[†] Vidhya M. Dev, and Jarad A. Mason*

Cite This: J. Am. Chem. Soc. 2022, 144, 6493−6503
Read Online

ABSTRACT: Barocaloric effects—thermal changes in a material induced by applied hydrostatic pressure—offer promise for creating solid-state refrigerants as alternatives to conventional volatile refrigerants. To enable efficient and scalable barocaloric cooling, materials that undergo high-entropy, reversible phase transitions in the solid state in response to a small change in pressure are needed. Here, we report that pressure-induced spin-crossover (SCO) transitions in the molecular iron(II) complex $Fe[HB(tz)_3]_2$ ($HB(tz)_3^-$ = bis[hydrotris(1,2,4-triazol-1-yl)borate]) drive giant and reversible barocaloric effects at easily accessible pressures. Specifically, high-pressure calorimetry and powder X-ray diffraction studies reveal that pressure shifts as low as 10 bar reversibly induce nonzero isothermal entropy changes, and a pressure shift of 150 bar reversibly induces a large isothermal entropy change (>90 J kg^{-1} K^{-1}) and adiabatic temperature change (>2 K). Moreover, we demonstrate that the thermodynamics of the SCO transition can be fine-tuned through systematic deuteration of the tris(triazolyl)borate ligand. These results provide new insights into pressure-induced SCO transitions and further establish SCO materials as promising barocaloric materials.

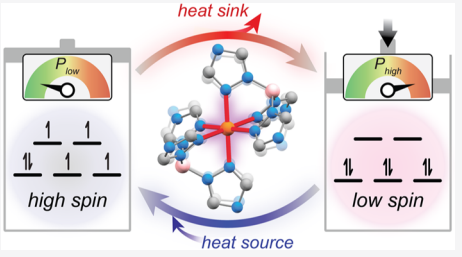

INTRODUCTION

With nearly 5 billion refrigerators, air conditioners, and heat pumps in operation around the world, the cooling sector consumes 20% of the global electricity supply.[1] To support population growth and improved standards of living amid an ever-warming climate, the demand for cooling is predicted to increase dramatically over the next several decades.[2] The energy spent on cooling the insides of buildings, for instance, is projected to triple by 2050.[3] Moreover, most cooling systems employ volatile hydrofluorocarbon (HFC) refrigerants—many of which have global warming potentials exceeding 2000 times that of CO_2—that are expected to become a major direct contributor to global greenhouse gas emissions (10−40%) by 2050 because of leakage into the atmosphere.[4,5] Given the lack of environmentally benign refrigerants that are also safe and energy efficient,[6] new approaches are urgently needed to provide sustainable cooling technologies that can be part of a net-zero global greenhouse gas emission future.[7]

Solid-state cooling through caloric effects—isothermal entropy or adiabatic temperature changes in a material induced by the application and removal of an external field—has emerged as a promising alternative to conventional vapor-compression cooling.[8−10] Caloric effects can be induced by a wide array of external stimuli, including magnetic fields,[11] electric fields,[12,13] and mechanical stress.[14−16] Barocaloric effects, which result from mechanical stress generated by a change in hydrostatic pressure, have recently received significant attention owing to their inherent advantages for realizing solid-state cooling at scale.[15−17] For instance, the generation of pressure is relatively straightforward compared to creating large magnetic or electric fields and is not intrinsically limited by the size of the working material.[18] Moreover, pressure-induced thermal responses in solids can be very large—particularly when they are associated with a first-order phase transition—and can even approach the entropy changes found in high-performance HFC refrigerants.[19,20]

Barocaloric effects originate from the coupling between certain degrees of freedom within a material and its volume and are thus strongest for materials that undergo sharp transitions between two states with large differences in entropy and volume.[15−17] In order for barocaloric effects to be driven reversibly with small shifts in pressure, solid−solid phase transitions must also exhibit minimal thermal hysteresis (ΔT_{hys}) and high sensitivity to pressure (dT/dP).[21] Although barocaloric effects have been reported for a wide variety of solid materials,[16,17] it has been challenging to identify barocaloric materials that do not require high operating pressures (often well over 500 bar) to induce reversible isothermal entropy (ΔS_{it}) and adiabatic temperature (ΔT_{ad}) changes of sufficient magnitude to drive a practical cooling cycle.[22] Thus, previous studies have focused on evaluating barocaloric effects at high pressures (>300 bar, Table S1), and

Received: February 2, 2022
Published: April 1, 2022

https://doi.org/10.1021/jacs.2c01315
J. Am. Chem. Soc. 2022, 144, 6493−6503

direct investigations into the magnitudes—and reversibility—of pressure-induced thermal changes at easily accessible pressures are rarely reported. Furthermore, much remains to be understood about the specific structural and chemical factors that influence barocaloric effects at a molecular level.

In 2016, spin-crossover (SCO) transitions were proposed as a promising mechanism to induce large barocaloric effects.[23] Most commonly observed in octahedral Fe(II) complexes, SCO typically describes a transition between a diamagnetic, low-spin (LS, $S = 0$) and a paramagnetic, high-spin (HS, $S = 2$) electronic configuration that can be triggered by temperature, pressure, or light.[24,25] Importantly, a thermally induced LS-to-HS transition—from the enthalpically favored LS state at lower temperatures to the entropically favored HS state at higher temperatures—is often accompanied by a large increase in entropy that results from access to more vibrational and electronic degrees of freedom, and a large increase in volume (generally 1−10%) that results from the lengthening of Fe−ligand bonds.[26] The large volume change renders SCO transitions sensitive to external pressure, with higher pressures favoring the contracted LS state and lower pressures favoring the expanded HS state.[27] Although several SCO materials have been predicted to exhibit strong barocaloric effects,[23,28−32] the exploration of SCO barocaloric materials remains in its infancy, and only two such compounds have been directly characterized through high-pressure calorimetry (Table S2).[33−35] Identifying the most promising candidate SCO materials for barocaloric cooling requires a greater understanding of how certain properties of SCO transitions—including entropy changes, volume changes, cooperativity, and hysteresis—influence the magnitude, reversibility, and pressure dependence of barocaloric effects. In pursuit of identifying an SCO material that displays large, reversible, and tunable barocaloric effects, we recognized that the molecular SCO complex $Fe[HB(tz)_3]_2$ ($HB(tz)_3^-$ = bis[hydrotris(1,2,4-triazol-1-yl)borate]) features a sharp—yet minimally hysteretic—SCO transition that is accompanied by a large change in entropy and volume.

Herein, we report that $Fe[HB(tz)_3]_2$ displays giant and highly reversible barocaloric effects. Through a combination of high-pressure calorimetry and powder X-ray diffraction (PXRD) experiments under both isobaric (variable temperature) and isothermal (variable pressure) conditions, we establish relationships between thermal properties, structural changes, and the reversibility of barocaloric effects during the SCO transition. Moreover, we investigate how the systematic deuteration of the tris(triazolyl)borate ligand affects the thermodynamics and pressure dependence of the SCO transition.

RESULTS AND DISCUSSION

Since the initial observation of an abrupt SCO transition in 2008,[36,37] $Fe[HB(tz)_3]_2$ has been extensively studied for its solvatomorphism,[38] thermal properties,[39] mechanical properties,[40] fast transition kinetics,[41] and amenability to thin-film deposition.[42] To the best of our knowledge, however, the effect of hydrostatic pressure on $Fe[HB(tz)_3]_2$—and its potential for barocaloric cooling—has not yet been investigated. Owing to its large entropy change (~100 J kg^{-1} K^{-1}), narrow hysteresis (<1 K),[38] and high thermal and chemical stability,[43] $Fe[HB(tz)_3]_2$ represents a particularly promising system for studying SCO-driven barocaloric effects.

Figure 1 illustrates how the pressure-induced SCO transition of $Fe[HB(tz)_3]_2$ could, in principle, be leveraged to drive a solid-state cooling cycle. In a Brayton-like cycle, a fast and adiabatic increase in pressure would first induce the HS-to-LS transition, and the thermal energy associated with this exothermic transition—not yet released to the surroundings—would increase the temperature of the material. The excess heat would then be dissipated into a heat sink, returning the material to its original temperature but in a contracted, lower entropy state. Upon the removal of pressure, $Fe[HB(tz)_3]_2$ would then undergo an endothermic LS-to-HS transition, and the decreased temperature of the material could be used to cool a heat source. Under such a cycle, the heat pumping process—from low-temperature heat source to high-temperature heat sink—is driven by the adiabatic temperature change (ΔT_{ad}). Alternatively, one can also envision switching the two spin states using pressure swings under isothermal conditions. Under this thermodynamic path (also known as a Stirling-like cycle), the isothermal entropy change (ΔS_{it}) determines the magnitude of thermal energy that can be pumped per cycle. Note that hybrid cooling cycles driven by pressure changes under both adiabatic and isothermal conditions can offer certain advantages for facilitating heat transfer and maximizing efficiency.[44] As such, the characterization of the magnitude of ΔT_{ad} and ΔS_{it} that can be induced by a given change in pressure is critical to the evaluation of barocaloric properties.

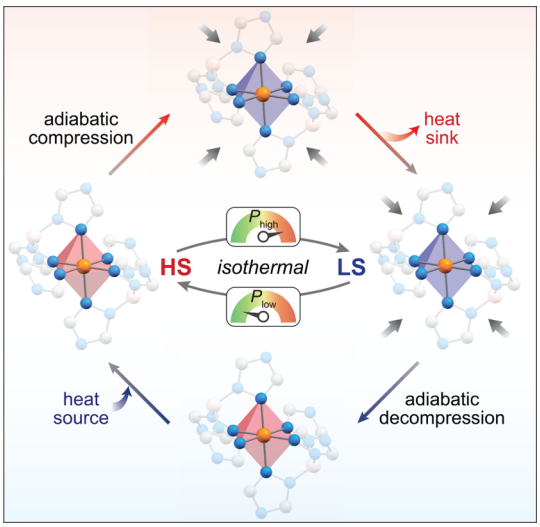

Figure 1. Illustration of how the pressure dependence of SCO transitions in the molecular SCO complex $Fe[HB(tz)_3]_2$ can be leveraged to drive a solid-state barocaloric cooling cycle.

As previously reported, $Fe[HB(tz)_3]_2$ undergoes a thermally induced phase change from a light-purple LS complex to an expanded colorless HS complex at 332 K.[37,38] During this transition, there is an average increase in the Fe−N bond lengths of 0.146 Å (7.3%), as determined from single-crystal structures obtained near the transition temperature (Figure 2a, Table S3). This leads to a 23.5 cm^3 kg^{-1} (3.6%) overall increase in the unit-cell volume, which is consistent with the 20(3) cm^3 kg^{-1} volume change, ΔV_{SCO}, directly measured via He pycnometry. Note that the volume expansion is highly anisotropic, occurring mostly along the crystallographic c axis despite relatively uniform Fe−N bond elongation (Figures S1−S3). Crystal packing shows a slight distortion in the hydrogen-bonding network upon SCO that occurs predominantly along the c axis (Figure S4), suggesting that the hydrogen bond directionality may be the cause of this

https://doi.org/10.1021/jacs.2c01315
J. Am. Chem. Soc. 2022, 144, 6493−6503

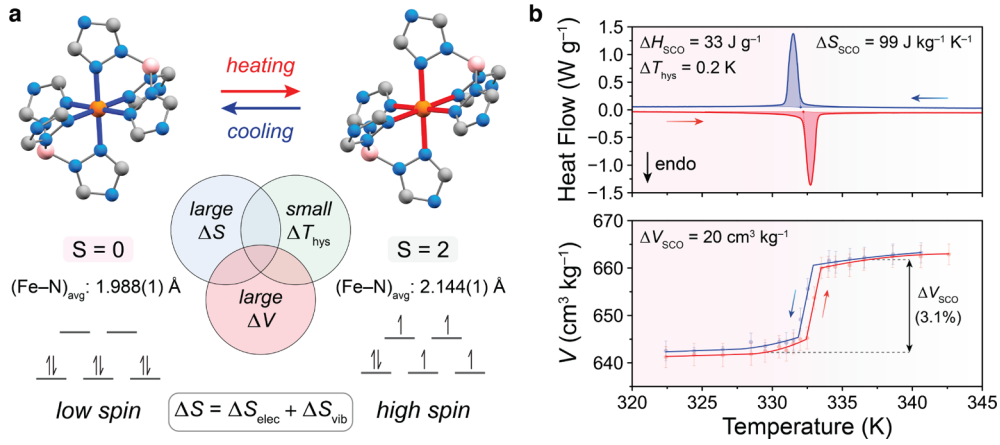

Figure 2. (a) $Fe[HB(tz)_3]_2$ undergoes a thermally induced SCO that is associated with an increase in electronic entropy (ΔS_{elec}) and vibrational entropy (ΔS_{vib}). (b) Ambient-pressure DSC with heating and cooling rates of 2 K min^{-1} (top) and He pycnometry (bottom) highlights the large entropy change, large volume change, and minimal hysteresis of the SCO transition.

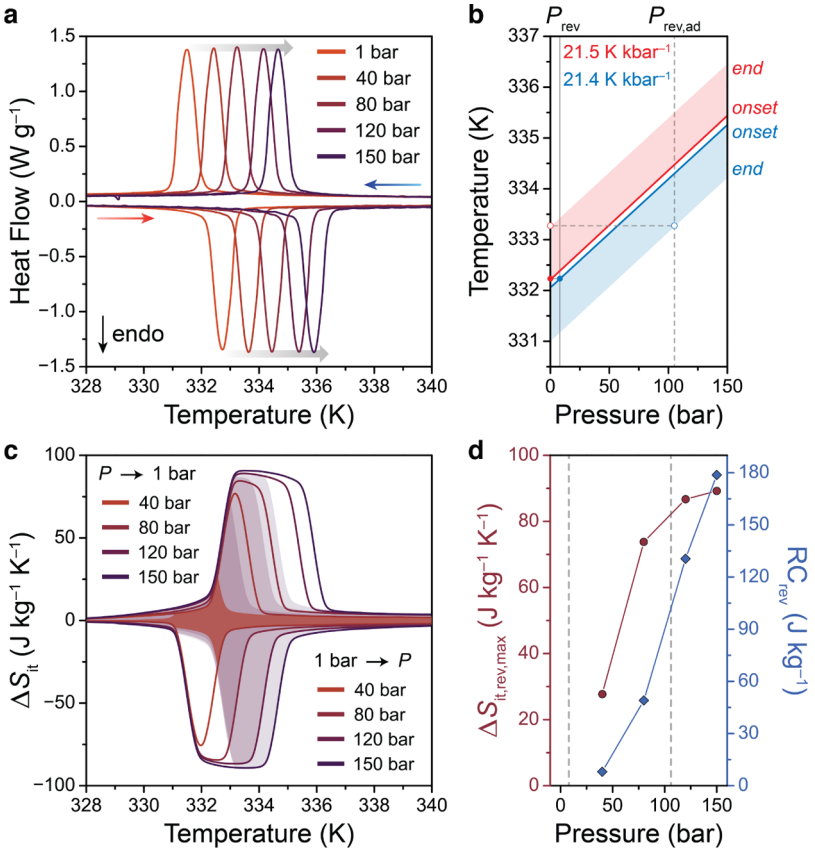

Figure 3. (a) DSC measurements for $Fe[HB(tz)_3]_2$ under applied hydrostatic pressure with heating and cooling rates of 2 K min^{-1} using He as the pressure-transmitting medium. (b) Pressure–temperature (P, T) phase diagram determined from the isobaric HP-DSC experiments. Phase boundaries were determined for both heating (red) and cooling (blue), with the transition width highlighted in the shaded area. Note that the minimum pressures required to drive a reversible isothermal entropy change (P_{rev}, 8 bar) and a reversible adiabatic temperature change ($P_{rev,ad}$, 106 bar) are indicated by vertical lines. (c) Isothermal entropy changes (ΔS_{it}) calculated by the quasi-direct method. The shaded area indicates the reversible isothermal entropy change ($\Delta S_{it,rev}$) that is accessible at each operating pressure. (d) The maximum reversible isothermal entropy change ($\Delta S_{it,rev,max}$) and reversible refrigeration capacity (RC_{rev}) are plotted as a function of operating pressure.

anisotropy. At ambient pressure, differential scanning calorimetry (DSC) experiments show that $Fe[HB(tz)_3]_2$ undergoes a sharp, reversible phase transition at 332 K with an enthalpy change (ΔH_{SCO}) of 33 J g^{-1} (16 kJ mol^{-1}), an entropy change (ΔS_{SCO}) of 99 J kg^{-1} K^{-1} (48 J mol^{-1} K^{-1}), and thermal hysteresis of just 0.2 K (Figure 2b), which agrees well with previously reported values.[38] Because the increased degeneracy of electronic configurations in the HS state is responsible for a 13.4 J mol^{-1} K^{-1} increase in entropy (as given by $\Delta S_{elec} = R \ln[(2S_{HS} + 1)/(2S_{LS} + 1)]$), roughly 70% of the total ΔS_{SCO} can be attributed to changes in vibrational entropy from changes in metal–ligand vibrations.[38,45] Note that octahedrally

https://doi.org/10.1021/jacs.2c01315
J. Am. Chem. Soc. 2022, 144, 6493–6503

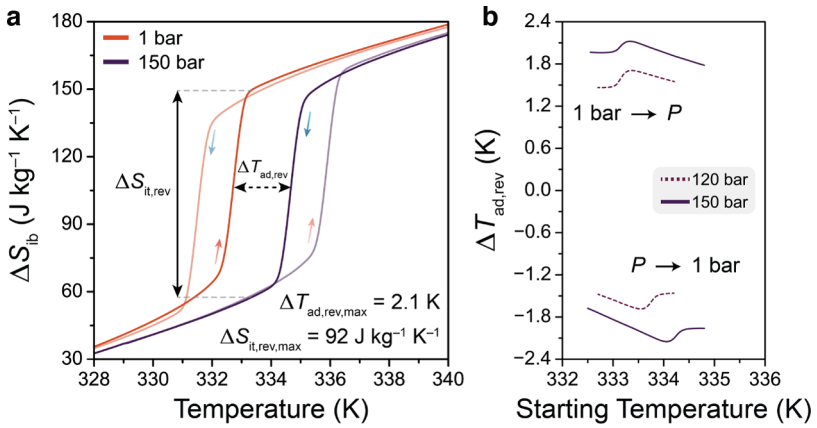

Figure 4. (a) Isobaric entropy changes (ΔS_{ib}) during heating at 1 bar and cooling at 150 bar for $Fe[HB(tz)_3]_2$. The thermodynamic paths used to evaluate $\Delta S_{it,rev}$ and $\Delta T_{ad,rev}$ are indicated by arrows. Note that these entropy curves take into account contributions from the additional entropy change outside of the transition (ΔS_+), calculated using $\Delta S_+ = -[(\partial V/\partial T)_{P=0}]\Delta P$, where V and ΔP denote specific volume and driving pressure, respectively. (b) $\Delta T_{ad,rev}$ is plotted as a function of starting temperature at 120 and 150 bar operating pressures.

coordinated complexes of transition metals in a d^6 electronic configuration achieve the maximal ΔS_{elec} during an SCO transition.

Pressure Dependence of the SCO Transition of $Fe[HB(tz)_3]_2$. From the Clausius–Clapeyron relationship ($dT/dP = \Delta V_{SCO}/\Delta S_{SCO}$), the pressure sensitivity of the SCO transition (dT/dP) is estimated to be 19.8 ± 3.2 K kbar^{-1}, which is a relatively high value among SCO materials.[23,27] To directly probe the pressure dependence, we carried out high-pressure DSC (HP-DSC) experiments under isobaric conditions up to 150 bar using He as the pressure-transmitting medium (Figure 3a). As expected, the phase transition onset shifts to higher temperatures with increasing pressure, with dT/dP of 21.5 ± 0.3 K kbar^{-1} during heating and 21.4 ± 0.5 K kbar^{-1} during cooling (Figures 3b, S5), which agrees well with the value predicted from the Clausius–Clapeyron equation. Importantly, the peak width and thermal hysteresis remain unchanged over this pressure range, and ΔS_{SCO} at 150 bar is within 97% of its ambient pressure value (Figure S6). Moreover, the spin transition remains robust even after 50 thermal cycles at 150 bar pressure (Figure S7).

To evaluate the reversibility of the pressure-induced spin transitions, we first calculated P_{rev} and $P_{rev,ad}$, which correspond to the minimum pressure required to induce a partial phase transition reversibly—overcoming thermal hysteresis—and to induce a complete phase transition reversibly—overcoming the entire hysteresis loop, including the transition width.[21] As such, P_{rev} corresponds to the pressure required to shift the onset of the exothermic transition (HS to LS) by ΔT_{hys} to coincide with the onset of the endothermic transition (LS to HS) at 1 bar and can be determined by

$$P_{rev} = \Delta T_{hys}/(dT/dP)_{cooling} \quad (1)$$

To capture the full entropy of the SCO transition reversibly under cyclic conditions, the exothermic transition peak needs to be shifted even further to overcome the transition peak width (ΔT_{width}) associated with both the endothermic and exothermic transitions. The minimum pressure for this condition, which is also the minimum pressure required to induce a reversible adiabatic temperature change, is determined by

$$P_{rev,ad} = (\Delta T_{hys} + \Delta T^{exo}_{width} + \Delta T^{endo}_{width})/(dT/dP)_{cooling} \quad (2)$$

The calculation of these values can be readily visualized on a phase diagram where both the transition onset and completion temperatures are shown as a function of pressure (Figure 3b). Because of its low thermal hysteresis, sharp transition width, and high pressure sensitivity, $Fe[HB(tz)_3]_2$ displays extremely low P_{rev} and $P_{rev,ad}$ values of 8 bar and 106 bar, respectively. To the best of our knowledge, this represents the lowest P_{rev} ever reported for a barocaloric material (Table S1).

Evaluation of Barocaloric Effects. To evaluate the magnitude of reversible barocaloric effects that can be induced in $Fe[HB(tz)_3]_2$ for a given shift in pressure, we used quasi-direct methods to obtain entropy curves from isobaric calorimetry experiments, which allow ΔS_{it} and ΔT_{ad} to be calculated along isothermal and adiabatic thermodynamic paths, respectively.[46] Note that quasi-direct methods have been commonly used to evaluate barocaloric effects owing to the challenge of maintaining strictly isothermal and adiabatic conditions during variable-pressure calorimetry experiments. In a quasi-direct analysis, isobaric entropy curves (ΔS_{ib}) are first obtained by integrating the baseline-subtracted DSC peaks (Figure S6). The resulting $\Delta S_{ib}(T, P)$ curves, which do not include contributions from the heat capacity outside of the phase transition region, represent the entropy near the phase transition as a function of temperature and pressure and emphasize the contribution of the first-order SCO transition. The isothermal entropy change associated with the pressure-induced SCO transition thus corresponds to the difference between isobaric entropy curves at ambient pressure, P_0, and applied pressure, P. To calculate ΔS_{it} for the endothermic LS-to-HS transition (induced by decompression), ΔS_{ib} curves obtained from endothermic transitions (induced by heating) are used

$$\Delta S_{it}(P \rightarrow P_0) = \Delta S_{ib,heating}(T, P_0) - \Delta S_{ib,heating}(T, P) \quad (3)$$

For the HS-to-LS transition induced by compression, ΔS_{ib} curves obtained from exothermic transitions (induced by cooling) are used

https://doi.org/10.1021/jacs.2c01315
J. Am. Chem. Soc. 2022, 144, 6493–6503

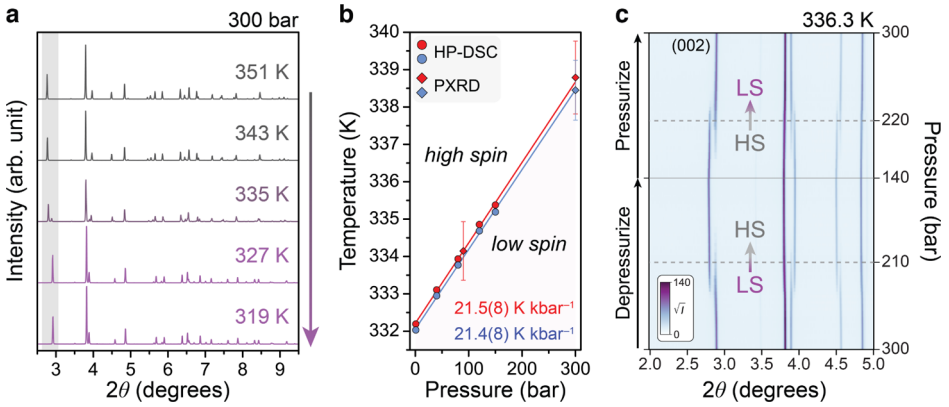

Figure 5. (a) Variable-temperature PXRD patterns for $Fe[HB(tz)_3]_2$ at 300 bar of He obtained during cooling. (b) Pressure dependence of the spin-transition temperature as determined by HP-DSC (circles) and PXRD (diamonds). (c) Isothermal, variable-pressure PXRD patterns show that the spin transition can be reversibly induced by a small shift in pressure with minimal pressure hysteresis. The pressures used to determine the width of the pressure hysteresis loop are marked with dashed lines. Note that an X-ray wavelength of 0.45185 Å was used for these synchrotron PXRD experiments.

$$\Delta S_{it}(P_0 \rightarrow P) = \Delta S_{ib,cooling}(T, P) - \Delta S_{ib,cooling}(T, P_0) \quad (4)$$

The resulting ΔS_{it} curves indicate that a small shift in pressure is sufficient to induce a large ΔS_{it}, with an applied pressure of just 40 bar leading to an irreversible ΔS_{it} of 77 J kg^{-1} K^{-1} (78% of ΔS_{SCO}) (Figure 3c).

For pressure-induced SCO transitions to occur reversibly under cyclic conditions, a reversible temperature range—over which both the exothermic and endothermic transitions are accessible—is necessary. This condition, which is met for applied pressures exceeding P_{rev}, ensures that at least some fraction of the material can be reversibly converted between HS and LS phases irrespective of the direction of the pressure change. Reversible isothermal entropy changes, $\Delta S_{it,rev}$, can be calculated from the overlap between compression-induced and decompression-induced ΔS_{it} curves reflected across the temperature axis, as highlighted in the shaded areas of Figure 3c. Excitingly, the maximum values of $\Delta S_{it,rev}$ curves ($\Delta S_{it,rev,max}$) plotted as a function of operating pressure illustrate that a substantial magnitude of $\Delta S_{it,rev}$ (28 J kg^{-1} K^{-1}) can be induced at just 40 bar and that 87 J kg^{-1} K^{-1} (88% of ΔS_{SCO}) can be reversibly captured at 120 bar (Figure 3d). The reversibility of barocaloric effects can also be evaluated by plotting the reversible refrigeration capacity (RC_{rev})—also known as the relative cooling power[11,47]—as a function of pressure. RC_{rev} takes into account the temperature range over which $\Delta S_{it,rev}$ is accessible and is defined as $\Delta S_{it,rev,max} \times \Delta T_{FWHM}$, where ΔT_{FWHM} is the full width at the half maximum of the $\Delta S_{it,rev}$ curves (Table S4). Notably, the magnitudes of $\Delta S_{it,rev}$ and RC_{rev} that can be realized in $Fe[HB(tz)_3]_2$ for a given pressure change, $\Delta S_{it,rev}/\Delta P$ and $RC_{rev}/\Delta P$, are competitive with leading barocaloric materials (Table S1).

We further analyze the reversibility of barocaloric effects by evaluating the magnitude of reversible adiabatic temperature changes, $\Delta T_{ad,rev}$, as a function of operating pressure. The isobaric hysteresis loop associated with $\Delta S_{ib}(T)$ at 150 bar is shifted well above the hysteresis loop associated with $\Delta S_{ib}(T)$ at 1 bar (Figure 4a). This creates a temperature window between the 1 bar heating and 150 bar cooling curves within which reversible adiabatic temperature changes are accessible (Figure S9). In Figure 4b, the increase in temperature induced by compression, $\Delta T_{ad,rev}(P_0 \rightarrow P)$, and the decrease in temperature induced by decompression, $\Delta T_{ad,rev}(P \rightarrow P_0)$, are plotted as a function of starting temperature. The $\Delta T_{ad,rev}$ curves show that adiabatic temperature changes of 1.7 and 2.1 K can be reversibly induced at 120 and 150 bar, respectively. Note that the isobaric entropy curves take into account contributions from heat capacity (c_p), including the additional entropy changes (ΔS_+) outside of the region of the first-order transition, calculated using $\Delta S_+ = -[(\partial V/\partial T)_{P=0}]\Delta P$, where V and ΔP denote specific volume and driving pressure, respectively. Although the contribution of ΔS_+ is relatively small at this pressure range (−2 J kg^{-1} K^{-1} at 150 bar), this entropy contribution is expected to substantially enhance the magnitude of barocaloric effects at higher pressures.[20,35] It is worth mentioning that the temperature span for a cooling cycle is not necessarily limited by the magnitude of $\Delta T_{ad,rev}$, and much larger temperature lifts can be established through regeneration schemes.[48,49] In addition, at pressures near 1 kbar, the magnitude of ΔT_{ad} for $Fe[HB(tz)_3]_2$ is predicted to reach up to 22 K, which is the maximum possible value estimated through $\Delta T_{ad,max} = -T\Delta S_{it}/c_p$.

To compare the barocaloric properties of $Fe[HB(tz)_3]_2$ to previously reported caloric materials, we also calculated a coefficient of refrigerant performance (CRP), defined as CRP = $|\Delta T_{ad,rev}\Delta S_{it,rev}/W|$, which describes the efficiency of caloric materials for converting input work W into reversible thermal changes (approximated as $\Delta T_{ad,rev}\Delta S_{it,rev}$).[47,50,51] Note that, for barocaloric materials, W represents the positive mechanical work done on the solid-state refrigerant and can be calculated as $W = 1/2P\Delta V$.[52] Using the maximum values for $\Delta T_{ad,rev}$ and $\Delta S_{it,rev}$ at 150 bar, we obtain a CRP of 1.3, which is highly competitive with the CRP value of 1.5−1.8 for the trinuclear SCO complex $Fe_3(bntrz)_6(tcnset)_6$ calculated over the pressure range of 300−2600 bar.[35] We note that direct comparison with this compound is not possible owing to the difference in the pressure range over which the reversible barocaloric effects were evaluated. Overall, the CRP value for $Fe[HB(tz)_3]_2$ is among the largest reported for any caloric material (Table S1),[18,51,53] further supporting the SCO transition as a compelling mechanism for caloric cooling.

***In Situ* Powder X-ray Diffraction.** To investigate the structural changes associated with the SCO transition of $Fe[HB(tz)_3]_2$ at high pressures, we performed *in situ* PXRD experiments. Although high-pressure XRD studies on a single

https://doi.org/10.1021/jacs.2c01315
J. Am. Chem. Soc. 2022, 144, 6493−6503

crystal of $Fe[HB(tz)_3]_2$ in the LS state were recently reported up to 26 kbar,[40] the effects of pressure on the HS state and the SCO transition have not yet been evaluated. Using the transition onset temperatures determined from isobaric PXRD experiments (Figures 5a, S12, S13), we were able to extend the (P, T) phase diagram for $Fe[HB(tz)_3]_2$ to 300 bar (Figure 5b). Over this extended range, the pressure dependence of the SCO transition is still linear, with a dT/dP of 21.5 ± 0.8 and 21.4 ± 0.8 K kbar^{-1} during heating and cooling, respectively. These values show excellent agreement with those determined from isobaric HP-DSC experiments from 1−150 bar (Figure 3b). Moreover, the crystallographic volume change at 300 bar of 22.1 cm^3 kg^{-1} (3.4%) is very close to that at ambient pressure (Figure S15). Even at high pressures, the volume change is still highly anisotropic, with $\Delta c/c$ = 4.8% across the SCO transition at 300 bar, while $\Delta a/a$ = −1.8% and $\Delta b/b$ = 0.6% (Figure S16). We anticipate that the anisotropic volume expansion—in combination with the strong preferred orientation of thin films (c axis normal to the substrate)[42]—may lead to large elastocaloric effects (thermal changes in response to uniaxial stress).[16,18]

Isothermal variable-pressure PXRD experiments were performed at 336 K to evaluate the reversibility of SCO transitions under conditions more relevant to barocaloric cooling cycles. Based on the extended (P, T) phase diagram, we predicted that pressure shifts of around 160 bar—while maintaining isothermal conditions at 336 K—would be sufficient to drive both the forward and reverse SCO transitions in full during pressure cycling. To ensure that isothermal conditions were maintained throughout the data collection, the sample was equilibrated for at least 3−5 min after each pressure change of 5−10 bar (Figure S17). As illustrated by the waterfall plot shown in Figure 5c, a pressure swing of 160 bar from 140 to 300 bar induced a complete conversion between HS and LS states in a reversible fashion. A pressure−volume (P−V) isotherm, which allows for the direct measurement of pressure hysteresis—rather than the thermal hysteresis that is evaluated during isobaric HP-DSC experiments—was then generated by determining precise unit-cell dimensions via Le Bail refinements (Figures 6, S18). The P−V isotherm contains an isothermal hysteresis loop with a width of 10 bar ($\Delta P_{hys,PXRD}$) and an isothermal volume change (ΔV_{it}) of 15.1 cm^3 kg^{-1} for the pressure-induced SCO transition. Given the uncertainty associated with extracting unit-cell parameters from powder patterns within the phase co-existence region, we estimate that the upper bound for the width of the hysteresis loop is 30 bar. It is worth emphasizing that isothermal hysteresis loops, which are more directly relevant to pressure-induced cooling cycles than isobaric hysteresis loops, are rarely reported for barocaloric materials that undergo first-order phase transitions,[54,55] presumably due to the challenge of inducing a fully reversible phase change at easily accessible pressures.

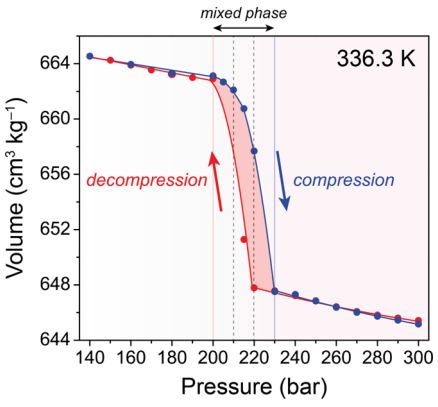

Figure 6. Pressure dependence of the specific volume of $Fe[HB(tz)_3]_2$ obtained from variable-pressure PXRD at 336.3 K. The P−V curves feature an isothermal hysteresis loop, with the enclosed area corresponding to the dissipated energy loss associated with hysteresis. The onset transition pressures during compression and decompression are marked with vertical dashed lines.

In addition to pressure hysteresis, the P−V isotherm enables a direct evaluation of efficiency loss due to hysteresis through the calculation of Δq_{diss}, which represents the dissipated energy due to hysteresis. Because the hysteresis loss represents the difference between energy stored during the compression-induced transition and energy released during the decompression-induced transition, Δq_{diss} corresponds to the enclosed area of the isothermal hysteresis loop. By approximating the enclosed area as a parallelogram, we obtained a Δq_{diss} of 15 J kg^{-1} using $\Delta q_{diss} = \Delta P_{hys,PXRD} \times \Delta V_{it}$ where $\Delta P_{hys,PXRD}$ and ΔV_{it} denote the width and height of the parallelogram, respectively. The efficiency loss due to hysteresis can then be quantified using a simple thermodynamic model that provides a direct relationship between the impact of Δq_{diss} (i.e., Δq_{diss} normalized by the maximum magnitude of a thermal change calculated as $\Delta S_{it,max}\Delta T_{ad,max}$) and the second-law efficiency (η) of a Carnot-like cycle[56]

$$\eta = \frac{\mathrm{COP}}{\mathrm{COP}_{\mathrm{Carnot}}} \approx \frac{1}{1 + 4\frac{\Delta q_{diss}}{\Delta S_{it,max}\Delta T_{ad,max}}} \quad (5)$$

The directly measured Δq_{diss} of 15 J kg^{-1} is just 0.7% of the $\Delta S_{it,max}\Delta T_{ad,max}$ of 2170 J kg^{-1} calculated from calorimetry data, which indicates that $Fe[HB(tz)_3]_2$—in an idealized thermodynamic cycle—could access a second-law efficiency of 97%. This analysis suggests that, at least at a material level, efficiency losses due to hysteresis will be minimal for $Fe[HB(tz)_3]_2$. We note that the dissipated energy due to hysteresis also reduces the cooling power of a cooling cycle by giving rise to the internal heating of the working material, as revealed by a recent modeling study.[55] Notably, this negative effect can be qualitatively compared across different types of caloric materials through quantifying the relative contribution of additional entropy generation due to hysteresis, ΔS_{hys} (calculated as $\Delta q_{diss}/T$), to the maximum isothermal entropy change $\Delta S_{it,max}$. This ratio $\Delta S_{hys}/\Delta S_{it,max}$—although seemingly small for most caloric materials (1−5%)—has a substantial influence on reducing cooling performance.[55] The $\Delta S_{hys}/\Delta S_{it,max}$ directly measured for $Fe[HB(tz)_3]_2$ is 0.05%. To the best of our knowledge, this value is the lowest ever reported for a caloric material,[55] which indicates that the impact of hysteresis on cooling power—in addition to the second-law efficiency—should be very small for $Fe[HB(tz)_3]_2$.

Beyond its relationship to efficiency losses, Δq_{diss} provides insight into the fatigue life of caloric materials through $\Delta q_{diss}/E_{input}$—a dimensionless quantity that represents the ratio between Δq_{diss} and the stored energy provided by the input work (E_{input}).[57] Specifically, studies of magneto-, electro-, and elastocaloric materials have suggested that materials with $\Delta q_{diss}/E_{input}$ below 10% tend to display extended cycle lifetimes (often greater than 10^6 cycles).[58] This empirical relationship,

https://doi.org/10.1021/jacs.2c01315
J. Am. Chem. Soc. 2022, 144, 6493−6503

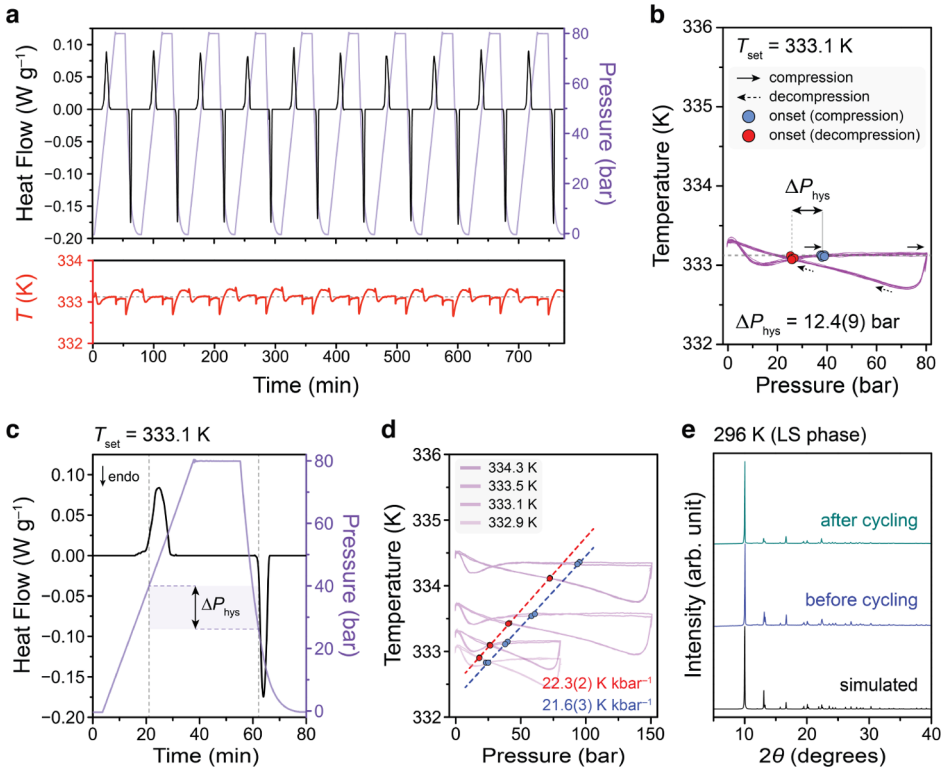

Figure 7. (a) Direct evaluation of pressure-induced spin transitions for $Fe[HB(tz)_3]_2$ through quasi-isothermal DSC experiments. Heat flow signals (top) and temperatures (bottom) were measured as a function of time during 10 cycles of applying and removing a hydrostatic pressure of 80 bar at 331.1 K with N_2 as the pressure-transmitting medium. (b) The pressure and temperature of the sample during the pressure cycling experiment are plotted, and the onset pressures and temperatures for compression-induced exotherms and decompression-induced endotherms are marked with blue and red circles, respectively. (c) Pressure hysteresis (ΔP_{hys}) is calculated as the difference between the onset pressures and is indicated by a horizontal purple bar. (d) Pressure–temperature phase diagram is mapped by measuring the temperature dependence of onset pressures via quasi-isothermal DSC experiments, with red and blue dashed lines corresponding to phase boundaries for decompression-induced LS-to-HS and compression-induced HS-to-LS transitions, respectively. (e) PXRD pattern after the pressure cycling experiments. The simulated powder pattern takes into account a [001] preferred orientation.

in agreement with the conventional view that smaller hysteresis in phase-transforming materials gives rise to less degradation and longer lifetimes,[59,60] highlights the importance of minimizing Δq_{diss} at the lowest E_{input} possible. The stored energy can be estimated as the $P-V$ work provided to the material when the forward transition is induced by a pressure shift of ΔP_{input}, with $E_{input} = \Delta P_{input} \times \Delta V_{it}$. Overall, the dissipated energy ratio can then be expressed by a relatively simple relationship

$$\frac{\Delta q_{diss}}{E_{input}} \approx \frac{\Delta P_{hys,PXRD}\Delta V_{it}}{\Delta P_{input}\Delta V_{it}} = \frac{\Delta P_{hys,PXRD}}{\Delta P_{input}} \quad (6)$$

Notably, the experimentally determined $\Delta P_{hys,PXRD}$ of 10 bar for a ΔP_{input} of 160 bar at 336 K yields an estimated $\Delta q_{diss}/E_{input}$ of ~6%, which suggests that $Fe[HB(tz)_3]_2$ should be able to sustain its functionality upon extended pressure cycling. This is consistent with a recent demonstration of $>10^7$ thermally induced SCO transition cycles for $Fe[HB(tz)_3]_2$ at ambient pressure.[43] Overall, the relatively low value of Δq_{diss} directly measured through isothermal PXRD experiments will motivate future efforts to evaluate its barocaloric performance at the device level.

Quasi-Isothermal HP-DSC. Although PXRD experiments enabled us to investigate the pressure dependence and reversibility of SCO transitions in $Fe[HB(tz)_3]_2$ under isothermal conditions, PXRD does not provide any direct information about the magnitudes of SCO-driven thermal changes that can be induced during pressure cycling. To this end, we designed calorimetry experiments to directly evaluate pressure-induced SCO transitions under quasi-isothermal conditions. In these HP-DSC experiments, we measured heat flow signals over 10 cycles of pressure swings between 1 bar and 80 bar at 333.1 K (Figure 7a). These conditions were chosen because isothermal entropy change curves obtained from isobaric HP-DSC experiments (shown in Figure 3c) indicated that a large entropy change—approaching the full SCO transition entropy—should be accessible with just an 80 bar shift in pressure if the temperature is held at 333.1 K. Indeed, the area under the heat flow peaks corresponding to compression-induced exotherms and decompression-induced endotherms is 28 and 27 J g^{-1}, respectively, which correspond to the isothermal entropy changes of 85 and 82 J kg^{-1} K^{-1} (Table S5), respectively. These values are in excellent agreement with the maximum isothermal entropy changes of 85 J kg^{-1} K^{-1} calculated via the quasi-direct method at the same temperature (Figure S23). Note that—unlike the HP-PXRD experiments—these HP-DSC experiments are not rigorously isothermal because the sample temperature fluctuates to a small extent during pressure changes (<0.5 K during decompression and <0.2 K during compression). However, the sample temperature quickly returns to the set temperature (T_{set}) and was always within 0.1 K of T_{set} at the

https://doi.org/10.1021/jacs.2c01315
J. Am. Chem. Soc. 2022, 144, 6493–6503

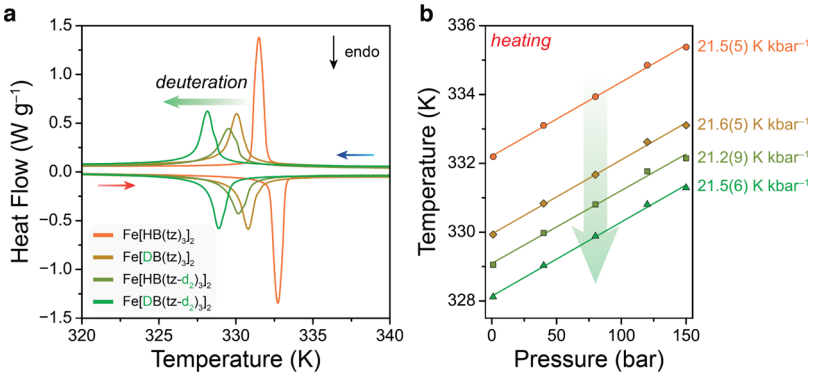

Figure 8. (a) Ambient-pressure DSC measurements with heating and cooling rates of 2 K min^{-1} using He as the pressure-transmitting medium show that deuteration lowers the spin transition temperature of $Fe[HB(tz)_3]_2$ with minimal impact on hysteresis. (b) The pressure dependence of the onset heating transition temperatures determined by HP-DSC are compared for deuterated complexes.

onset of the SCO transition (Figure 7b), hence the classification of these experiments as quasi-isothermal.

In addition to entropy changes, pressure hysteresis ($\Delta P_{hys,DSC}$) can also be directly evaluated from the quasi-isothermal HP-DSC experiments as the difference between transition onset pressures during compression and decompression, with $\Delta P_{hys,DSC} = P_{tr,comp} - P_{tr,decomp}$ (Figure 7c). Importantly, the directly measured $\Delta P_{hys,DSC}$ of 12.4 ± 0.9 bar is in excellent agreement with the predicted value of 10 bar from isobaric HP-DSC experiments carried out under N_2 (Figure S24). To further establish the validity of the quasi-isothermal DSC experiments, we carried out pressure cycling at three additional temperatures (332.9, 333.5, and 334.3 K) to map out phase boundaries on a (P, T) diagram for the pressure-induced SCO transition (Figures 7d, S26–28). As expected, the phase boundaries coincide well with those determined from isobaric HP-DSC experiments (Figure S29), with dT/dP values of 22.3 ± 0.2 and 21.6 ± 0.3 K $kbar^{-1}$ for decompression and compression, respectively. Furthermore, the horizontal width between the phase boundaries—which corresponds to pressure hysteresis—ranges from 10.8 to 11.4 bar. These results confirm that the temperature control throughout the quasi-isothermal experiments is of sufficient quality to accurately measure the temperature dependence of transition pressures.

The pressure hysteresis measured by isothermal HP-DSC is in good agreement with that measured by PXRD experiments, even with the different experimental conditions of continuous pressure scans from 0 to 80 bar for the former measurements and discrete pressure steps from 140 to 300 bar for the latter (Table S6). Overall, these results highlight the excellent low-pressure reversibility of $Fe[HB(tz)_3]_2$. Moreover, we found that pressure cycling does not impact the crystallinity or crystal morphology of the sample, as evidenced by PXRD patterns (Figure 7e) and scanning electron microscopy (SEM) images (Figure S25).

Systematic Deuteration. Given their high sensitivity to the electronic and steric environments surrounding transition metal centers, SCO transitions can be readily tuned through ligand functionalization.[24,61−63] One of the simplest ways of manipulating SCO transitions is through isotopic substitution, with the deuteration of organic ligands, for example, leading to subtle—yet direct—perturbations in vibrational properties, electronic properties, and intermolecular interactions that can substantially shift the SCO temperature. Indeed, the molecular SCO complexes $[Fe(2\text{-pic})_3]Cl_2$·solvent (solvent = MeOH or EtOH)[64] and $[Fe(5\text{-}NO_2\text{)-sal-N(1,4,7,10)}]$[65] exhibit increases in the SCO transition temperatures of 15 and 10 K, respectively, after deuteration. Deuteration can also decrease the SCO temperature, as has been observed for the coordination polymer $Fe(pyridine)_2[Ni(CN)_4]$[66] and the molecular complex $[FeL_2][BF_4]_2$ (L = 2,6-di(pyrazol-1-yl)-pyridine),[33] which exhibit decreases of 8 and 5 K, respectively, after deuteration.

Inspired by these previous studies, we systematically replaced hydrogen atoms in $Fe[HB(tz)_3]_2$ with deuterium to evaluate the effect of deuteration on the SCO transition thermodynamics and pressure dependence (Figure S30). Isobaric HP-DSC experiments on the three additional complexes $Fe[DB(tz)_3]_2$, $Fe[HB(tz\text{-}d_2)_3]_2$, and $Fe[DB(tz\text{-}d_2)_3]_2$ revealed that T_{SCO} shifts downward as the degree of deuteration increases, with full deuteration lowering T_{SCO} by 4 K (Figure 8). Deuteration, however, has a negligible impact on the pressure sensitivity (Figure 8b) and thermal hysteresis (Table S7) of the SCO transition. Interestingly, replacement of B−H with B−D has a greater impact on T_{SCO} than triazole deuteration on a per D basis, even though the B−H moiety does not directly participate in intermolecular hydrogen bonding in the solid state (Figure S4).[38] Comparison of molar ΔH_{SCO} and ΔS_{SCO} suggests that, in all cases, deuteration leads to a lowering of both ΔH_{SCO} and ΔS_{SCO}, yet the enthalpic decrease is more than the entropic decrease, which leads to an overall decrease in T_{SCO} (Table S7). Note that, on a gravimetric basis, the fully deuterated complex still displays a large ΔS_{SCO} (86 J kg^{-1} K^{-1}) that is about 87% of ΔS_{SCO} for the original complex. In addition, the negligible impact of deuteration on dT/dP suggests that ΔV_{SCO} slightly decreases upon deuteration because $dT/dP = \Delta V_{SCO}/\Delta S_{SCO}$ according to the Clausius−Clapeyron relationship. These trends point to interesting relationships between intermolecular interactions, vibrational properties, and phase-change thermodynamics, and efforts to investigate the microscopic origins of these effects—and those induced by other ligand functionalization strategies—are currently in progress.

■ CONCLUSIONS

The foregoing results demonstrate giant and reversible barocaloric effects in $Fe[HB(tz)_3]_2$ and further establish SCO transitions as a promising mechanism for solid-state barocaloric cooling. As shown through comprehensive high-pressure calorimetry and diffraction experiments, the high-

https://doi.org/10.1021/jacs.2c01315
J. Am. Chem. Soc. 2022, 144, 6493−6503

pressure sensitivity and low hysteresis of this molecular SCO complex enable large and reversible barocaloric effects to be realized with very small shifts in hydrostatic pressure. Moreover, isotopic labeling can be used to fine-tune the SCO temperature without compromising reversibility. Given the exceptionally high stability, switching endurance, and compatibility with vacuum deposition that distinguish $Fe[HB(tz)_3]_2$ from other SCO materials, we anticipate that this system may provide unique opportunities for harnessing barocaloric effects in thermal devices spanning multiple length scales.

■ ASSOCIATED CONTENT

Supporting Information

The Supporting Information is available free of charge at https://pubs.acs.org/doi/10.1021/jacs.2c01315.

Additional experimental details, high-pressure calorimetry data, entropy curves used to evaluate barocaloric effects, PXRD data, single-crystal XRD data, and summary of all the structural and thermodynamic data (PDF)

Accession Codes

CCDC 2149760−2149761 contain the supplementary crystallographic data for this paper. These data can be obtained free of charge via www.ccdc.cam.ac.uk/data_request/cif, or by emailing data_request@ccdc.cam.ac.uk, or by contacting The Cambridge Crystallographic Data Centre, 12 Union Road, Cambridge CB2 1EZ, UK; fax: +44 1223 336033.

■ AUTHOR INFORMATION

Corresponding Author

Jarad A. Mason − *Department of Chemistry and Chemical Biology, Harvard University, Cambridge, Massachusetts 02138, United States;* orcid.org/0000-0003-0328-7775; Email: mason@chemistry.harvard.edu

Authors

Jinyoung Seo − *Department of Chemistry and Chemical Biology, Harvard University, Cambridge, Massachusetts 02138, United States*

Jason D. Braun − *Department of Chemistry and Chemical Biology, Harvard University, Cambridge, Massachusetts 02138, United States;* orcid.org/0000-0002-5850-8048

Vidhya M. Dev − *Department of Chemistry and Chemical Biology, Harvard University, Cambridge, Massachusetts 02138, United States*

Complete contact information is available at: https://pubs.acs.org/10.1021/jacs.2c01315

Author Contributions

†J.S. and J.D.B. contributed equally to this work.

Notes

The authors declare no competing financial interest.

■ ACKNOWLEDGMENTS

This research was partially supported by the NSF through the Harvard University Materials Research Science and Engineering Center DMR-2011754. Additional support was provided by the Climate Change Solutions Funds at Harvard University and by the Arnold and Mabel Beckman Foundation through the Beckman Young Investigator grant awarded to J.A.M. We also thank the Korea Foundation for Advanced Studies for a graduate fellowship awarded to J.S. PXRD data were collected on beamline 17-BM at the Advanced Photon Source at Argonne National Laboratory, which is supported by the U.S. Department of Energy, Office of Science, Office of Basic Energy Sciences under Contract no. DE-AC02-06CH11357. We thank Dr. Andrey A. Yakovenko for assisting with HP-PXRD experiments, Daniel Erdosy for assisting with SEM experiments, and Adam Slavney for assisting with He pycnometry measurements.

■ REFERENCES

(1) Dupont, J. L.; Domanski, P.; Lebrun, P.; Ziegler, F. *38th Note on Refrigeration Technologies: The Role of Refrigeration in the Global Economy*; International Institute of Refrigeration (IIR), 2019.

(2) Davis, L. W.; Gertler, P. J. Contribution of Air Conditioning Adoption to Future Energy Use under Global Warming. *Proc. Natl. Acad. Sci. U.S.A.* **2015**, *112*, 5962−5967.

(3) The Future of Cooling: Opportunities for Energy Efficient Air Conditioning; International Energy Agency. 2018, https://www.iea.org/reports/the-future-of-cooling (accessed March 3, 2022).

(4) McLinden, M. O.; Brown, J. S.; Brignoli, R.; Kazakov, A. F.; Domanski, P. A. Limited Options for Low-Global-Warming-Potential Refrigerants. *Nat. Commun.* **2017**, *8*, 14476.

(5) Velders, G. J. M.; Fahey, D. W.; Daniel, J. S.; McFarland, M.; Andersen, S. O. The Large Contribution of Projected HFC Emissions to Future Climate Forcing. *Proc. Natl. Acad. Sci. U.S.A.* **2009**, *106*, 10949−10954.

(6) McLinden, M. O.; Seeton, C. J.; Pearson, A. New Refrigerants and System Configurations for Vapor-Compression Refrigeration. *Science* **2020**, *370*, 791−796.

(7) Net Zero by 2050; International Energy Agency. 2021, https://www.iea.org/reports/net-zero-by-2050 (accessed March 3, 2022).

(8) Takeuchi, I.; Sandeman, K. Solid-State Cooling with Caloric Materials. *Phys. Today* **2015**, *68*, 48−54.

(9) Greco, A.; Aprea, C.; Maiorino, A.; Masselli, C. A Review of the State of the Art of Solid-State Caloric Cooling Processes at Room-Temperature before 2019. *Int. J. Refrig.* **2019**, *106*, 66−88.

(10) Moya, X.; Mathur, N. D. Caloric Materials for Cooling and Heating. *Science* **2020**, *370*, 797−803.

(11) Gschneidner, K. A.; Pecharsky, V. K. Magnetocaloric Materials. *Annu. Rev. Mater. Sci.* **2000**, *30*, 387−429.

(12) Scott, J. F. Electrocaloric Materials. *Annu. Rev. Mater. Res.* **2011**, *41*, 229−240.

(13) Shi, J.; Han, D.; Li, Z.; Yang, L.; Lu, S.-G.; Zhong, Z.; Chen, J.; Zhang, Q. M.; Qian, X. Electrocaloric Cooling Materials and Devices for Zero-Global-Warming-Potential, High-Efficiency Refrigeration. *Joule* **2019**, *3*, 1200−1225.

(14) Wang, R.; Fang, S.; Xiao, Y.; Gao, E.; Jiang, N.; Li, Y.; Mou, L.; Shen, Y.; Zhao, W.; Li, S.; Fonseca, A. F.; Galvão, D. S.; Chen, M.; He, W.; Yu, K.; Lu, H.; Wang, X.; Qian, D.; Aliev, A. E.; Li, N.; Haines, C. S.; Liu, Z.; Mu, J.; Wang, Z.; Yin, S.; Lima, M. D.; An, B.; Zhou, X.; Liu, Z.; Baughman, R. H. Torsional Refrigeration by Twisted, Coiled, and Supercoiled Fibers. *Science* **2019**, *366*, 216−221.

(15) Mañosa, L.; Planes, A. Materials with Giant Mechanocaloric Effects: Cooling by Strength. *Adv. Mater.* **2017**, *29*, 1603607.

(16) Cazorla, C. Novel Mechanocaloric Materials for Solid-State Cooling Applications. *Appl. Phys. Rev.* **2019**, *6*, 041316.

(17) Boldrin, D. Fantastic Barocalorics and Where to Find Them. *Appl. Phys. Lett.* **2021**, *118*, 170502.

(18) Mañosa, L.; Planes, A. Solid-State Cooling by Stress: A Perspective. *Appl. Phys. Lett.* **2020**, *116*, 050501.

(19) Li, B.; Kawakita, Y.; Ohira-Kawamura, S.; Sugahara, T.; Wang, H.; Wang, J.; Chen, Y.; Kawaguchi, S. I.; Kawaguchi, S.; Ohara, K.; Li, K.; Yu, D.; Mole, R.; Hattori, T.; Kikuchi, T.; Yano, S.-i.; Zhang, Z.; Zhang, Z.; Ren, W.; Lin, S.; Sakata, O.; Nakajima, K.; Zhang, Z. Colossal Barocaloric Effects in Plastic Crystals. *Nature* **2019**, *567*, 506−510.

(20) Lloveras, P.; Aznar, A.; Barrio, M.; Negrier, P.; Popescu, C.; Planes, A.; Mañosa, L.; Stern-Taulats, E.; Avramenko, A.; Mathur, N. D.; Moya, X.; Tamarit, J.-L. Colossal Barocaloric Effects near Room Temperature in Plastic Crystals of Neopentylglycol. *Nat. Commun.* **2019**, *10*, 1803.
(21) Aznar, A.; Lloveras, P.; Barrio, M.; Negrier, P.; Planes, A.; Mañosa, L.; Mathur, N. D.; Moya, X.; Tamarit, J.-L. Reversible and Irreversible Colossal Barocaloric Effects in Plastic Crystals. *J. Mater. Chem. A* **2020**, *8*, 639−647.
(22) Moya, X.; Ilevbare, I. M. Materials for the Energy Transition Roadmap: Caloric Energy Conversion Materials; Henry Royce Institute. 2020, https://www.royce.ac.uk/content/uploads/2021/10/M4ET-Caloric-Energy-Conversion-Materials-roadmap.pdf (accessed 2022-03-03).
(23) Sandeman, K. G. Research Update: The Mechanocaloric Potential of Spin Crossover Compounds. *APL Mater.* **2016**, *4*, 111102.
(24) Gütlich, P.; Goodwin, H. A. Spin Crossover—An Overall Perspective. In *Spin Crossover in Transition Metal Compounds I*; Gütlich, P., Goodwin, H. A., Eds.; Topics in Current Chemistry; Springer Berlin Heidelberg: Berlin, Heidelberg, 2004; Vol. *233*, pp 1−47.
(25) Real, J. A.; Gaspar, A. B.; Muñoz, M. C. Thermal, Pressure and Light Switchable Spin-Crossover Materials. *Dalton Trans.* **2005**, 2062−2079.
(26) Guionneau, P. Crystallography and Spin-Crossover. A View of Breathing Materials. *Dalton Trans.* **2014**, *43*, 382−393.
(27) Gaspar, A. B.; Molnár, G.; Rotaru, A.; Shepherd, H. J. Pressure Effect Investigations on Spin-Crossover Coordination Compounds. *Compt. Rendus Chem.* **2018**, *21*, 1095−1120.
(28) von Ranke, P. J. A Microscopic Refrigeration Process Triggered through Spin-Crossover Mechanism. *Appl. Phys. Lett.* **2017**, *110*, 181909.
(29) von Ranke, P. J.; Alho, B. P.; Ribas, R. M.; Nobrega, E. P.; Caldas, A.; de Sousa, V. S. R.; Colaço, M. V.; Marques, L. F.; Rocco, D. L.; Ribeiro, P. O. Colossal Refrigerant Capacity in $[Fe(hyptrz)_3]$-$A_2 \cdot H_2O$ Around the Freezing Temperature of Water. *Phys. Rev. B* **2018**, *98*, 224408.
(30) von Ranke, P. J.; Alho, B. P.; Nobrega, E. P.; Caldas, A.; de Sousa, V. S. R.; Colaço, M. V.; Marques, L. F.; Rocha, G. M.; Rocco, D. L.; Ribeiro, P. O. The Refrigerant Capacity in Spin-Crossover Materials: Application to [Fe(phen)2(NCS)2]. *J. Magn. Magn.* **2019**, *489*, 165421.
(31) von Ranke, P. J.; Alho, B. P.; da Silva, P. H. S.; Ribas, R. M.; Nobrega, E. P.; de Sousa, V. S. R.; Colaço, M. V.; Marques, L. F.; Reis, M. S.; Scaldini, F. M.; Escobar, L. B. L.; Ribeiro, P. O. Large Barocaloric Effect in Spin-Crossover Complex $[CrI_2(depe)_2]$. *J. Appl. Phys.* **2020**, *127*, 165104.
(32) von Ranke, P. J.; Alho, B. P.; da Silva, P. H. S.; Ribas, R. M.; Nobrega, E. P.; de Sousa, V. S. R.; Carvalho, A. M. G.; Ribeiro, P. O. Refrigeration through Barocaloric Effect Using the Spin Crossover Complex $\{Fe[H_2B(pz)_2]_2(bipy)\}$. *Phys. Status Solidi B* **2021**, *258*, 2100108.
(33) Vallone, S. P.; Tantillo, A. N.; dos Santos, A. M.; Molaison, J. J.; Kulmaczewski, R.; Chapoy, A.; Ahmadi, P.; Halcrow, M. A.; Sandeman, K. G. Giant Barocaloric Effect at the Spin Crossover Transition of a Molecular Crystal. *Adv. Mater.* **2019**, *31*, 1807334.
(34) Pittala, N.; Thétiot, F.; Charles, C.; Triki, S.; Boukheddaden, K.; Chastanet, G.; Marchivie, M. An Unprecedented Trinuclear Fe^{II} Triazole-Based Complex Exhibiting a Concerted and Complete Sharp Spin Transition above Room Temperature. *Chem. Commun.* **2017**, *53*, 8356−8359.
(35) Romanini, M.; Wang, Y.; Gürpinar, K.; Ornelas, G.; Lloveras, P.; Zhang, Y.; Zheng, W.; Barrio, M.; Aznar, A.; Gràcia-Condal, A.; Emre, B.; Atakol, O.; Popescu, C.; Zhang, H.; Long, Y.; Balicas, L.; Lluís Tamarit, J.; Planes, A.; Shatruk, M.; Mañosa, L. Giant and Reversible Barocaloric Effect in Trinuclear Spin-Crossover Complex $Fe_3(bntrz)_6(tcnset)_6$. *Adv. Mater.* **2021**, *33*, 2008076.
(36) Janiak, C.; Scharmann, T. G.; Green, J. C.; Parkin, R. P. G.; Kolm, M. J.; Riedel, E.; Mickler, W.; Elguero, J.; Charamunt, R. M.; Sanz, D. Effects of Nitrogen Substitution in Poly(pyrazolyl)borato Ligands: From Orbital Energy Levels to C-H··· O Hydrogen Bonding. *Chem.—Eur. J.* **1996**, *2*, 992−1000.
(37) van Koningsbruggen, P. J.; Miller, J. S. Observation of a 331 K (58 °C) Spin Transition for bis[hydrotris(1,2,4-triazol-1-yl)borate]-iron(II) by Variable Temperature Infrared Spectroscopy and Magnetic Susceptibility Measurements. *Solid State Sci.* **2008**, *10*, 1804−1806.
(38) Rat, S.; Ridier, K.; Vendier, L.; Molnár, G.; Salmon, L.; Bousseksou, A. Solvatomorphism and Structural-Spin Crossover Property Relationship in Bis[hydrotris(1,2,4-triazol-1-yl)borate]iron-(II). *CrystEngComm* **2017**, *19*, 3271−3280.
(39) Ridier, K.; Zhang, Y.; Piedrahita-Bello, M.; Quintero, C. M.; Salmon, L.; Molnár, G.; Bergaud, C.; Bousseksou, A. Heat Capacity and Thermal Damping Properties of Spin-Crossover Molecules: A New Look at an Old Topic. *Adv. Mater.* **2020**, *32*, 2000987.
(40) Mikolasek, M.; Manrique-Juarez, M. D.; Shepherd, H. J.; Ridier, K.; Rat, S.; Shalabaeva, V.; Bas, A.-C.; Collings, I. E.; Mathieu, F.; Cacheux, J.; Leichle, T.; Nicu, L.; Nicolazzi, W.; Salmon, L.; Molnár, G.; Bousseksou, A. Complete Set of Elastic Moduli of a Spin-Crossover Solid: Spin-State Dependence and Mechanical Actuation. *J. Am. Chem. Soc.* **2018**, *140*, 8970−8979.
(41) Ridier, K.; Rat, S.; Shepherd, H. J.; Salmon, L.; Nicolazzi, W.; Molnár, G.; Bousseksou, A. Spatiotemporal Dynamics of the Spin Transition in $[Fe(HB(tz)_3)_2]$ Single Crystals. *Phys. Rev. B* **2017**, *96*, 134106.
(42) Shalabaeva, V.; Rat, S.; Manrique-Juarez, M. D.; Bas, A.-C.; Vendier, L.; Salmon, L.; Molnár, G.; Bousseksou, A. Vacuum Deposition of High-Quality Thin Films Displaying Spin Transition near Room Temperature. *J. Mater. Chem. C* **2017**, *5*, 4419−4425.
(43) Ridier, K.; Bas, A.-C.; Zhang, Y.; Routaboul, L.; Salmon, L.; Molnár, G.; Bergaud, C.; Bousseksou, A. Unprecedented Switching Endurance Affords for High-Resolution Surface Temperature Mapping Using a Spin-Crossover Film. *Nat. Commun.* **2020**, *11*, 3611.
(44) Qian, S.; Geng, Y.; Wang, Y.; Ling, J.; Hwang, Y.; Radermacher, R.; Takeuchi, I.; Cui, J. A Review of Elastocaloric Cooling: Materials, Cycles and System Integrations. *Int. J. Refrig.* **2016**, *64*, 1−19.
(45) Molnár, G.; Niel, V.; Gaspar, A. B.; Real, J.-A.; Zwick, A.; Bousseksou, A.; McGarvey, J. J. Vibrational Spectroscopy of Cyanide-Bridged, Iron(II) Spin-Crossover Coordination Polymers: Estimation of Vibrational Contributions to the Entropy Change Associated with the Spin Transition. *J. Phys. Chem. B* **2002**, *106*, 9701−9707.
(46) Moya, X.; Kar-Narayan, S.; Mathur, N. D. Caloric Materials near Ferroic Phase Transitions. *Nat. Mater.* **2014**, *13*, 439−450.
(47) Griffith, L. D.; Mudryk, Y.; Slaughter, J.; Pecharsky, V. K. Material-Based Figure of Merit for Caloric Materials. *J. Appl. Phys.* **2018**, *123*, 034902.
(48) Brown, G. V. Magnetic Heat Pumping near Room Temperature. *J. Appl. Phys.* **1976**, *47*, 3673−3680.
(49) Steyert, W. A. Stirling-Cycle Rotating Magnetic Refrigerators and Heat Engines for Use Near Room Temperature. *J. Appl. Phys.* **1978**, *49*, 1216−1226.
(50) Wood, M. E.; Potter, W. H. General Analysis of Magnetic Refrigeration and Its Optimization Using a New Concept: Maximization of Refrigerant Capacity. *Cryogenics* **1985**, *25*, 667−683.
(51) Brück, E.; Yibole, H.; Zhang, L. A Universal Metric for Ferroic Energy Materials. *Philos. Trans. R. Soc., A* **2016**, *374*, 20150303.
(52) Crossley, S.; Mathur, N. D.; Moya, X. New Developments in Caloric Materials for Cooling Applications. *AIP Adv.* **2015**, *5*, 067153.
(53) Li, J.; Dunstan, D.; Lou, X.; Planes, A.; Mañosa, L.; Barrio, M.; Tamarit, J.-L.; Lloveras, P. Reversible Barocaloric Effects Over a Large Temperature Span in Fullerite C_{60}. *J. Mater. Chem. A* **2020**, *8*, 20354−20362.
(54) Moya, X.; Defay, E.; Heine, V.; Mathur, N. D. Too Cool to Work. *Nat. Phys.* **2015**, *11*, 202−205.

https://doi.org/10.1021/jacs.2c01315
J. Am. Chem. Soc. 2022, 144, 6493−6503

(55) Masche, M.; Ianniciello, L.; Tušek, J.; Engelbrecht, K. Impact of Hysteresis on Caloric Cooling Performance. *Int. J. Refrig.* **2021**, *121*, 302−312.
(56) Hess, T.; Maier, L. M.; Bachmann, N.; Corhan, P.; Schäfer-Welsen, O.; Wöllenstein, J.; Bartholomé, K. Thermal Hysteresis and Its Impact on the Efficiency of First-Order Caloric Materials. *J. Appl. Phys.* **2020**, *127*, 075103.
(57) Hou, H.; Qian, S.; Takeuchi, I. Materials, Physics, and Systems for Multicaloric Cooling. *Nat. Rev. Mater.* **2022**, DOI: 10.1038/s41578-022-00428-x.
(58) Hou, H.; Simsek, E.; Ma, T.; Johnson, N. S.; Qian, S.; Cissé, C.; Stasak, D.; Al Hasan, N.; Zhou, L.; Hwang, Y.; Radermacher, R.; Levitas, V. I.; Kramer, M. J.; Zaeem, M. A.; Stebner, A. P.; Ott, R. T.; Cui, J.; Takeuchi, I. Fatigue-Resistant High-Performance Elastocaloric Materials Made by Additive Manufacturing. *Science* **2019**, *366*, 1116−1121.
(59) Gutfleisch, O.; Gottschall, T.; Fries, M.; Benke, D.; Radulov, I.; Skokov, K. P.; Wende, H.; Gruner, M.; Acet, M.; Entel, P.; Farle, M. Mastering Hysteresis in Magnetocaloric Materials. *Philos. Trans. R. Soc., A* **2016**, *374*, 20150308.
(60) Song, Y.; Chen, X.; Dabade, V.; Shield, T. W.; James, R. D. Enhanced Reversibility and Unusual Microstructure of a Phase-Transforming Material. *Nature* **2013**, *502*, 85−88.
(61) Roubeau, O. Triazole-Based One-Dimensional Spin-Crossover Coordination Polymers. *Chem.—Eur. J.* **2012**, *18*, 15230−15244.
(62) Kimura, A.; Ishida, T. Spin-Crossover Temperature Predictable from DFT Calculation for Iron(II) Complexes with 4-Substituted Pybox and Related Heteroaromatic Ligands. *ACS Omega* **2018**, *3*, 6737−6747.
(63) Halcrow, M. A.; Capel Berdiell, I.; Pask, C. M.; Kulmaczewski, R. Relationship between the Molecular Structure and Switching Temperature in a Library of Spin-Crossover Molecular Materials. *Inorg. Chem.* **2019**, *58*, 9811−9821.
(64) Gütlich, P.; Köppen, H.; Steinhäuser, H. G. Deuterium Isotope Effect on the High-Spin ⇌ Low-Spin Transition in Deuterated Solvates of tris(2-picolylamine)iron(II) chloride. *Chem. Phys. Lett.* **1980**, *74*, 475−480.
(65) Bousseksou, A.; Tommasi, L.; Lemercier, G.; Varret, F.; Tuchagues, J.-P. Deuterium Isotope Effect in the Two-Step Spin-State Transition of $[Fe^{II}(5\text{-}NO_2\text{-sal-N}(1,4,7,10))]$ Investigated by Mössbauer Spectroscopy and Magnetic Susceptibility. *Chem. Phys. Lett.* **1995**, *243*, 493−499.
(66) Hosoya, K.; Kitazawa, T.; Takahashi, M.; Takeda, M.; Meunier, J.-F.; Molnár, G.; Bousseksou, A. Unexpected Isotope Effect on the Spin Transition of the Coordination Polymer $Fe(C_5H_5N)_2[Ni(CN)_4]$. *Phys. Chem. Chem. Phys.* **2003**, *5*, 1682−1688.

https://doi.org/10.1021/jacs.2c01315
J. Am. Chem. Soc. 2022, 144, 6493−6503